ADVANCED FUNCTIONAL MATERIALS
www.afm-journal.de

Imaging Dielectric Breakdown in Valence Change Memory

*William A. Hubbard, Jared J. Lodico, Ho Leung Chan, Matthew Mecklenburg, and Brian C. Regan**

Dielectric breakdown (DB) controls the failure, and increasingly the function, of microelectronic devices. Standard imaging techniques, which generate contrast based on physical structure, struggle to visualize this electronic process. Here in situ scanning transmission electron microscopy (STEM) electron beam-induced current (EBIC) imaging of DB in Pt/HfO_2/Ti valence change memory devices is reported. STEM EBIC imaging directly visualizes the electronic signatures of DB, namely local changes in the conductivity and in the electric field, with high spatial resolution and good contrast. DB is observed to proceed through two distinct structures arranged in series: a volatile, "soft" filament created by electron injection; and a non-volatile, "hard" filament created by oxygen-vacancy aggregation. This picture makes a physical distinction between "soft" and "hard" DB, while at the same time accommodating "progressive" DB, where the relative lengths of the hard and soft filaments can change on a continuum.

1. Introduction

Dielectric films, generally oxides, are key elements in all microelectronic devices.[1,2] The basic computing unit of the modern, information-based economy, the transistor, contains a dielectric film at its heart, as does the simple capacitor. Such films are also the switching component in the resistive random access memory (RRAM) elements that might soon constitute much of fast digital storage[2–4] and neuromorphic processors.[3,5] Depending on the application, conduction in nominally insulating dielectric films can be central to device function (RRAM) or failure (gate dielectrics, capacitors). The reliability of computing hardware, present and future, thus depends critically on the detailed mechanisms underlying controlled and uncontrolled dielectric breakdown (DB) in these insulators.

Because RRAM devices feature controlled DB[2,6–9] that can be switched ON and OFF repeatedly, they represent an ideal target for a study of DB. For oxide-based RRAM (known as valence change memory —VCM— or OxRAM) in particular, many details about the switching process are poorly understood. Unsettled issues involve the filament growth direction (toward the cathode[4,10–12] or away from it[13,14]), the filament conduction method,[15] and the filament morphology.[8,15] Incomplete understanding of the physics and chemistry that drive switching in VCM is the main obstacle to its optimization and commercialization.[3,15,16]

Direct imaging of DB in VCM has the potential to reveal critical details about the switching mechanisms, but visualizing a dynamic and fundamentally electronic process occurring inside a bulk solid is extremely challenging.[5] DB has been imaged using scanning probe microscopy (SPM),[17–21] scanning electron microscopy (SEM),[22–24] X-rays,[25,26] and transmission electron microscopy (TEM).[12,14,20,22,27–31] Standard SPM, SEM, X-ray, and TEM imaging are sensitive to physical structure: the arrangement of atoms,[22,24,27] and perhaps their chemical identities.[12,20,25–30,32] But the changes to the physical structure of an insulator can be millions of times smaller — and thus more difficult to visualize — than the changes to its electronic structure. For example, doping at a level of 10^{-5} can change the conductivity by a factor of 10^3.[33] Thus standard imaging techniques show DB in the limit where marked changes to the physical structure occur, such as bubbling,[17,18,22,24] clustering,[20,29,32] and crystallization.[20,22–24,27,31] This physically-stressed limit is not necessarily the regime of interest, especially in the case of RRAM, where the DB must be controlled and reversible.[24,27]

Electronic signatures of DB can be visualized with modified versions of the standard imaging techniques. Conductive atomic force microscopy (CAFM),[8,20] scalpel scanning probe microscopy,[19] scanning tunneling microscopy,[21] in situ TEM holography,[14] and electron beam-induced current imaging (EBIC) in an SEM[23] have been used to image changes to the local conductivity and electric fields associated with DB. However, these imaging technique struggle with poor perspective (spatial or temporal), imaging artifacts, and/or low contrast.[5] To date it has not been possible to perform high-contrast imaging of cycling in a clean VCM device at nm-scale resolution.

To address these issues we fabricate Pt/HfO_2/Ti VCM devices in a slant-vertical architecture (**Figure 1**) and then image them

W. A. Hubbard, J. J. Lodico, H. L. Chan, B. C. Regan
Department of Physics and Astronomy
University of California
Los Angeles, CA 90095, USA
E-mail: regan@physics.ucla.edu
W. A. Hubbard, J. J. Lodico, H. L. Chan, B. C. Regan
California NanoSystems Institute
University of California
Los Angeles, CA 90095, USA
M. Mecklenburg
Core Center of Excellence in Nano Imaging
University of Southern California
Los Angeles, CA 90089, USA

The ORCID identification number(s) for the author(s) of this article can be found under https://doi.org/10.1002/adfm.202102313.

DOI: 10.1002/adfm.202102313

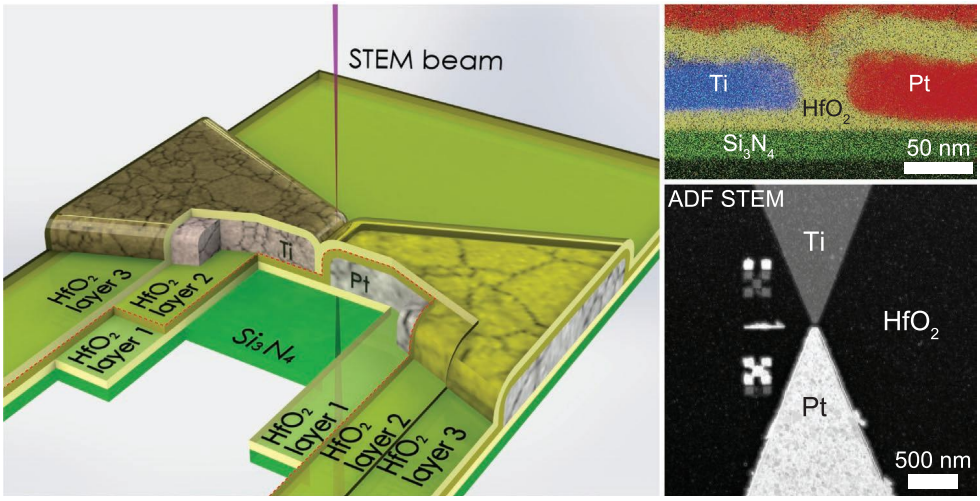

Figure 1. VCM slant-vertical device architecture. (left) A VCM device, shown entirely to-scale with cutaways, consists of ALD HfO_2, a Pt electrode, ALD HfO_2, a Ti electrode, and a capping layer of ALD HfO_2, deposited in this order on a Si_3N_4 support membrane. As highlighted by the red dotted line, sequential layer deposition ensures that, regardless of the horizontal gap, the electrodes are always separated by the second (conformal) layer of HfO_2. (Right top) X-ray energy dispersive spectroscopy (EDS) data from a FIB-prepared cross section of a slant-vertical device show its elemental composition (see also Figures S1 and S2, Supporting Information). None of our switching experiments use this point-of-view. (Right bottom) Low magnification ADF STEM shows a slant-vertical device in plan-view, the perspective adopted for all switching experiments.

using scanning transmission electron microscope (STEM) EBIC. Since its implementation as a high-κ gate dielectric in 2007, HfO_2 (hafnia) has been considered perhaps the preferred dielectric for transistor, flash memory, and RRAM applications.[7,16] The slant-vertical architecture maintains a realistic RRAM device topology while simultaneously allowing good TEM imaging access. This architecture has previously revealed the movement of Cu atoms (atomic number $Z = 29$) in Cu/Al_2O_3 conductive bridge memory (CBRAM) over multiple switching cycles.[34] However, the oxygen atom ($Z = 8$), or, more precisely, vacancy movement thought to mediate VCM switching[6,7,9,15] is too subtle to be detected in an Hf ($Z = 72$) background with standard TEM imaging. We therefore also image the slant-vertical VCM devices using STEM EBIC imaging. STEM EBIC imaging has two important contrast modes: the standard mode, which generates its contrast based on electron–hole pair separation,[35,36] and a recently-developed mode that generates contrast via the emission of secondary electrons (SEEBIC).[37] Because standard EBIC and SEEBIC imaging are sensitive to local electric fields[35,36] and to the local conductivity,[37,38] respectively, these imaging modalities are uniquely suited for mapping the effects of DB at high spatial resolution.[39]

2. Results and Discussion

As detailed below, we observe DB proceeding in two steps. Increasing the Ti–Pt bias voltage from zero first produces a volatile, or "soft," filament. This structure, which we attribute to charge injection into existing oxygen vacancies, vanishes when the bias voltage is removed. Further increasing the bias voltage eventually produces a non-volatile or "hard" filament. The hard filament, which we attribute to the production and aggregation of new oxygen vacancies, remains if the bias voltage is set to 0 V, but it can be dissolved by reversing the voltage bias. The hard filament conducts ohmically, while the soft filament conducts via the Poole-Frenkel (PF) mechanism. A complete filament puts the VCM device in the ON state and consists of distinct hard and soft filaments arranged in series, with the latter limiting the net electrical transport via PF conduction. These filaments can be associated with regions of hard and soft DB,[40] respectively.

A slant-vertical $Pt/HfO_2/Ti$ VCM device (Figure 1) imaged in plan-view affords a side-on perspective of the switching region.[34] The top (Ti) and bottom (Pt) electrodes are both completely encased in HfO_2, with a continuous HfO_2 layer separating them (see Section 1, Supporting Information). This architecture avoids the focused ion beam (FIB) sample preparation[12,14,22,28,29,32] often used to create cross-sectional TEM samples, which introduces additional, compromising interfaces, structural damage, and chemical (e.g., gallium) contamination that have the potential to alter the DB process under study.[5] Thus we have good STEM imaging access in clean, microfabricated devices with a realistic (i.e., vertically stacked) topology.

We cycle a device up to a potential just below the switching potential and then back to zero (**Figure 2**; Movie S1, Supporting Information). While the bias current is initially small, it is easily measured and increases exponentially, from 5 pA at 1 V, to 20 pA at 20 V, in this device (see also Figure 4). Annular dark field (ADF) STEM imaging of the device essentially maps the proton column density — the Pt ($Z = 78$) electrode generates more signal than the Ti ($Z = 22$) electrode (Figure 2, top row). (The Si_3N_4 and HfO_2 are very and mostly uniformly distributed, respectively, across this field of view.) Unsurprisingly, standard STEM ADF imaging of the device shows no changes as the device begins to conduct. Although cation motion has been observed in valence change chemistries,[21] the absence of ADF contrast changes like those seen in ref. [34] with a similar device architecture indicates that few, if any, of the heavy nuclei in the sample are relocating as a result of the applied potential.

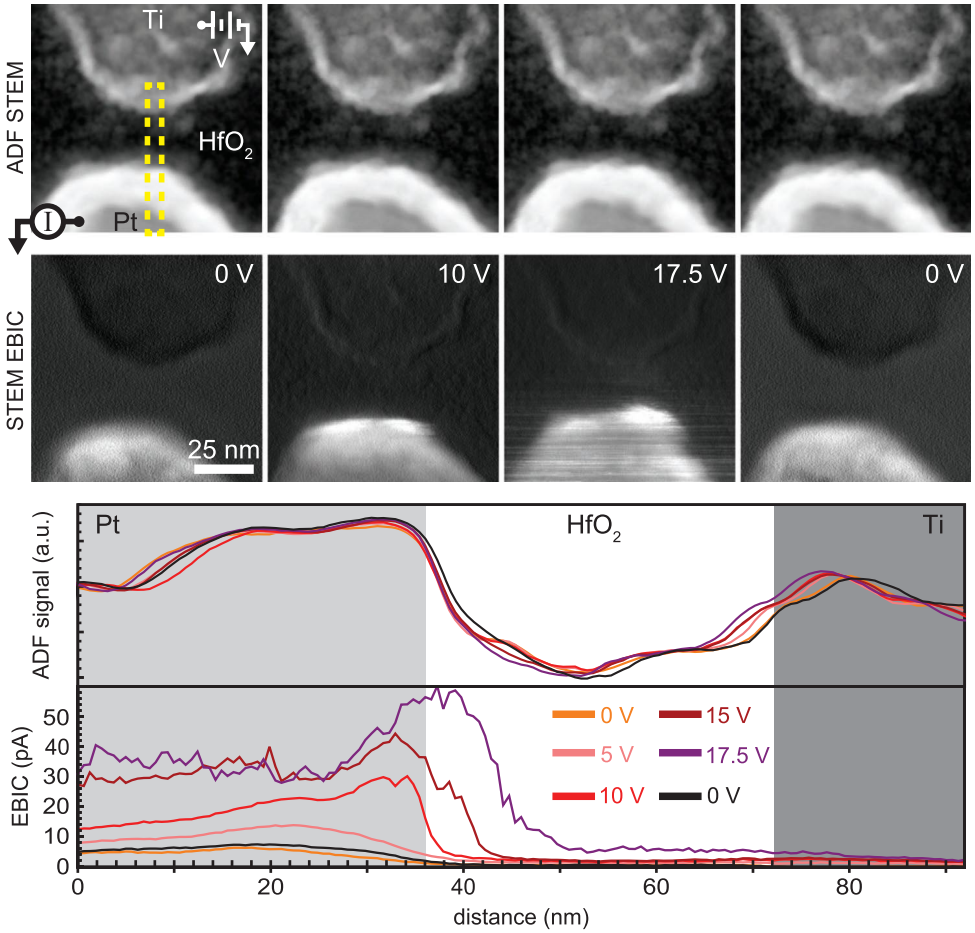

Figure 2. Soft filament formation and dissolution. (Top row) STEM ADF images of a slant-vertical Pt/HfO_2/Ti VCM device show no changes as the Ti–Pt bias voltage is increased. (Second row) Simultaneously acquired STEM EBIC images, on the other hand, show the region electrically connected to the Pt expanding into the gap. See also Movie S1, Supporting Information. (Bottom) Line profiles extracted from these images (and additional images from the same bias series not shown) by averaging over the rectangular region indicated in the first ADF image show these trends quantitatively. Symbols in the first ADF image indicate the electrical connections for applying the bias and measuring the EBIC.

STEM EBIC imaging (Figure 2, second row), on the other hand, reveals the VCM device's changing conductivity and connectivity landscape.[37] In the device's OFF state the Pt electrode is well-isolated from the Ti and thus is only connected to the transimpedance amplifier (TIA) that measures the EBIC. When the beam is incident on the Pt, secondary electrons (SEs) are ejected from the sample, the holes left behind reach the TIA, and this positive current gives bright contrast. When the beam is incident on the Ti, SEs are also ejected, but the corresponding holes go to ground through the Ti. While the TIA does not register these holes, a portion of the emitted SEs are recaptured[37] in the Pt and the resulting negative current in the Pt produces dark contrast. When the beam is not incident on an electrode, few SEs are produced and the contrast resulting is a neutral gray.

Even subtle, pre-switching electronic changes are immediately visible with STEM EBIC imaging (Figure 2, second row). With no applied bias the Pt electrode has the same shape whether viewed with ADF or with EBIC, but as the bias is increased, the Pt electrode, viewed with EBIC, swells. With a 10 V bias, a bright region grows from the Pt edge toward the Ti. With 17.5 V applied, this bright region grows even closer to the Ti electrode, with an especially bright feature appearing at the apex of the protrusion slightly to the right of frame center. When the bias is removed, the bright structure disappears and the electrode, as viewed with STEM EBIC, reverts to its initial configuration. This structure is thus both conducting and volatile.

Line profiles (Figure 2, bottom) present these results more quantitatively. The ADF data (both images and line profiles) show no contrast changes as a function of increasing bias, other than some small shifts attributable to sample drift over the 90 s image-acquisition period. The corresponding EBIC data, however, show a conducting region that extends farther and farther into the gap, reaching almost halfway across at the final high bias of 17.5 V before disappearing entirely when the bias is returned to 0 V.

These volatile conducting structures ("soft" filaments) that form prior to switching (see also **Figure 3**; Figures S3 and S7 and Movies S1–S5, Supporting Information) appear under both Ti-Pt bias polarities and always grow from the cathode to anode (low to high potential), as expected for electron-charge

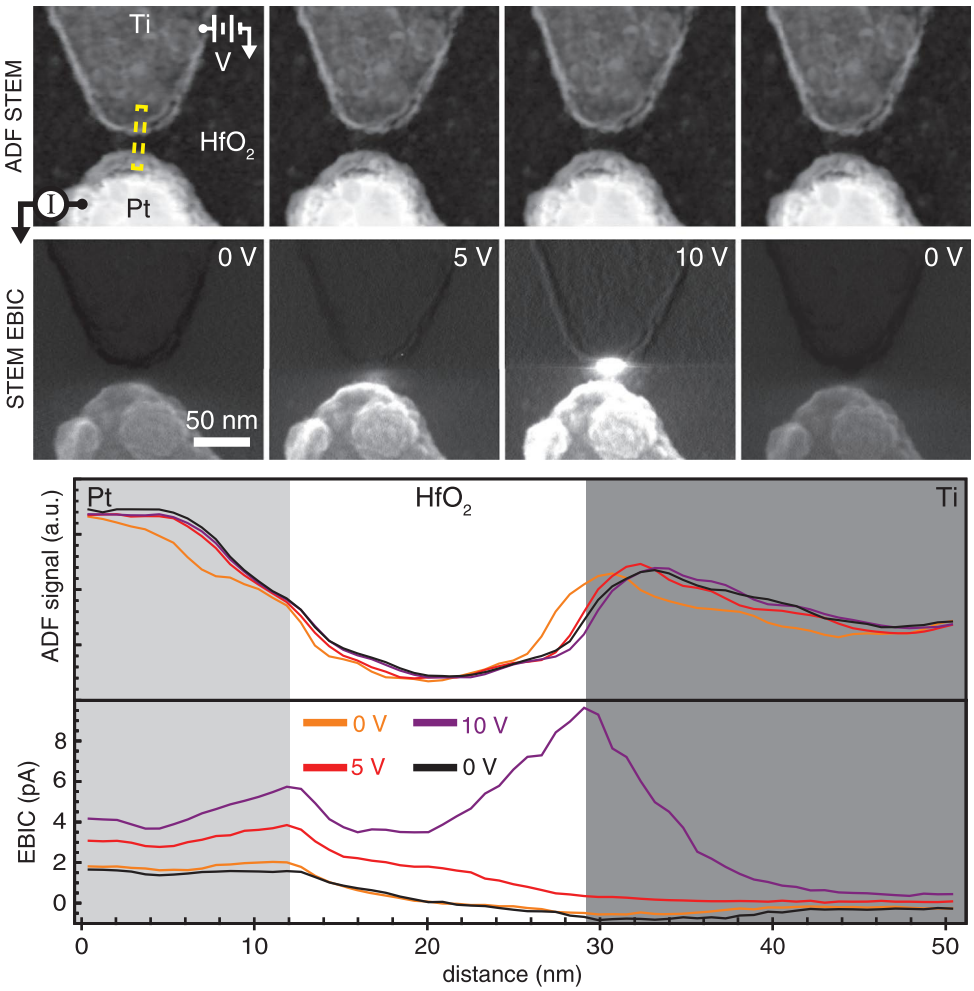

Figure 3. Large *E*-field at the switching point. (Top) STEM ADF imaging shows no changes as a Ti/HfO_2/Pt device is biased at 0, 5, and 10 V, and 0 V. (Second row) EBIC imaging shows a soft filament grow, almost connect, and then disappear. See also Movie S3, Supporting Information. (Bottom) Line profiles of the ADF and EBIC signals from the dashed yellow region indicated in the 0 V ADF image show the corresponding contrast values quantitatively. At non-zero bias, small device currents (e.g., 300 fA at 10 V) add to the EBIC (Figure S6, Supporting Information).

injection. With the Pt held at virtual ground, for example, a soft filament grows from the Pt under positive Ti bias and from the Ti under negative Ti bias (Figure S7, Supporting Information).

In the STEM EBIC images discussed above, the contrast is dominated by SEEBIC, which is generated by secondary electron emission. Standard EBIC contrast, on the other hand, is generated by the separation of electron–hole pairs in a local electric field *E*. As the soft filament extends across the gap, the local *E*-field increases like V/d, where V is the applied potential and d is the width of the remaining gap (Figure 3). At low potentials, SEEBIC dominates the contrast and shows the soft filament extending from the cathode (e.g., Figure 2 and first two columns of Figure 3). At high potentials the device is ON and cannot be EBIC-imaged under bias because the much-larger device current swamps the EBIC. However, in a very narrow, intermediate potential range, the *E*-field is large enough to separate electron–hole pairs, and yet not so large that device conduction saturates the TIA (Figure 3, third column). Here standard EBIC contrast dominates the SEEBIC contrast (see Figures S4 and S5, Supporting Information), vividly highlighting the large *E*-field in the region extending from the tip of the soft filament to the Ti electrode. (See also Figures S6, S7, S9, and Movies S2–S5, Supporting Information.) Line profiles show that the peak EBIC, and thus the peak *E*-field, is in fact at the Ti interface (Figure 3, bottom). Up to this point in the switching cycle, the observed changes are all volatile, in that returning the applied bias to 0 V causes the filamentary structures observed to disappear (Figure 3, fourth column).

Applying just over 20 V bias to the Ti electrode of the Figure 2 device causes it to transition from the high-resistance state (HRS) (rightmost Figure 2 = leftmost **Figure 4**) to the low-resistance state (LRS) (Figure 4 middle). The device current accordingly jumps to the pre-programmed current limit of 50 nA (Figure 4 plot).[34] Continuing the STEM EBIC image series of Figure 2 then becomes impossible because at high bias the ON-state device current saturates the TIA. Therefore we reduce the device bias voltage to zero for imaging.

While (again) no changes are seen with ADF, even without the applied bias STEM EBIC reveals that the transition to the LRS is accompanied by a change in the HfO_2: a new, conducting

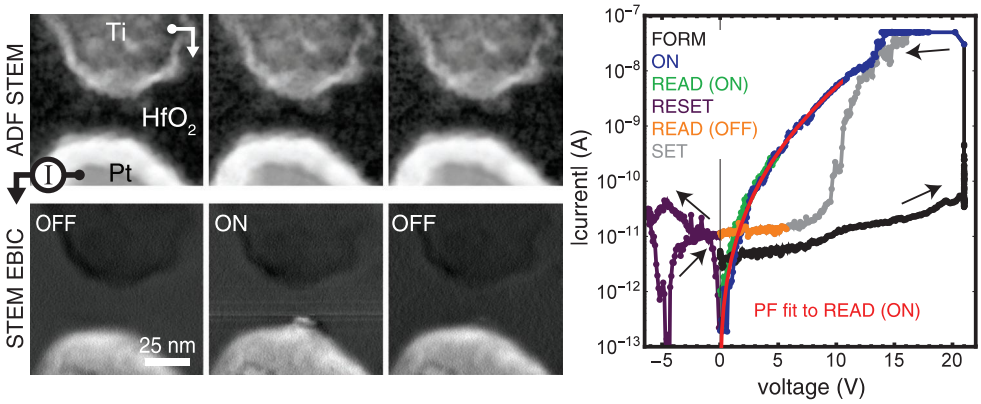

Figure 4. Hard filament formation and dissolution. ADF imaging (left, top row) shows no changes between the ON and OFF states of the VCM device of Figure 2. STEM EBIC imaging (left, bottom row), however, again shows obvious changes between the ON and OFF states, with the most marked being a sharp protuberance at the Pt electrode's apex. Each image is acquired after voltage programming (see text), but with a 0 V bias. The *I*–*V* plot (right) shows a complete cycle of this device. The LRS data is well fit by the PF model (red curve). The apparent "battery" (i.e., current $I \neq 0$ at voltage $V = 0$ and vice versa) in the HRS is an artifact of stray capacitance, the large device resistance, and the voltage ramp rate $dV/dt = 0.3$ V s^{-1}. Note that, because of device currents and beam sensitivity, STEM EBIC images cannot be directly associated with all points on the plot.

region electrically connected to the Pt electrode now extends into the gap. Since it appears at 0 V, by definition this change is non-volatile, or "hard", and it appears where the soft filament generates its most intense SEEBIC signal (Figure 2). The hard filament does not bridge the entire gap between electrodes (see also Figures S8, S10, S11, and S14, Supporting Information).

After a –10 V RESET, the device returns to the HRS and the hard filament is almost entirely dissolved (Figure 4 rightmost images). During subsequent cycles the hard filament reappears in the same region in the ON state and disappears (though perhaps incompletely) in the OFF state (Figure S8, Supporting Information).

The current–voltage (*I*–*V*) plot (Figure 4) shows a typical FORM/ON/READ/OFF/READ/SET cycle for this device. In the LRS, the transport is well-fit (see Section 1, Supporting Information) by the PF conduction model.[9,41,42] Evidence of PF conduction also appears when we image an ON-state device with STEM EBIC while floating the Ti electrode. We image a device after a RESET, after a SET, and again immediately afterward (**Figure 5**). For all three images the device is under no applied

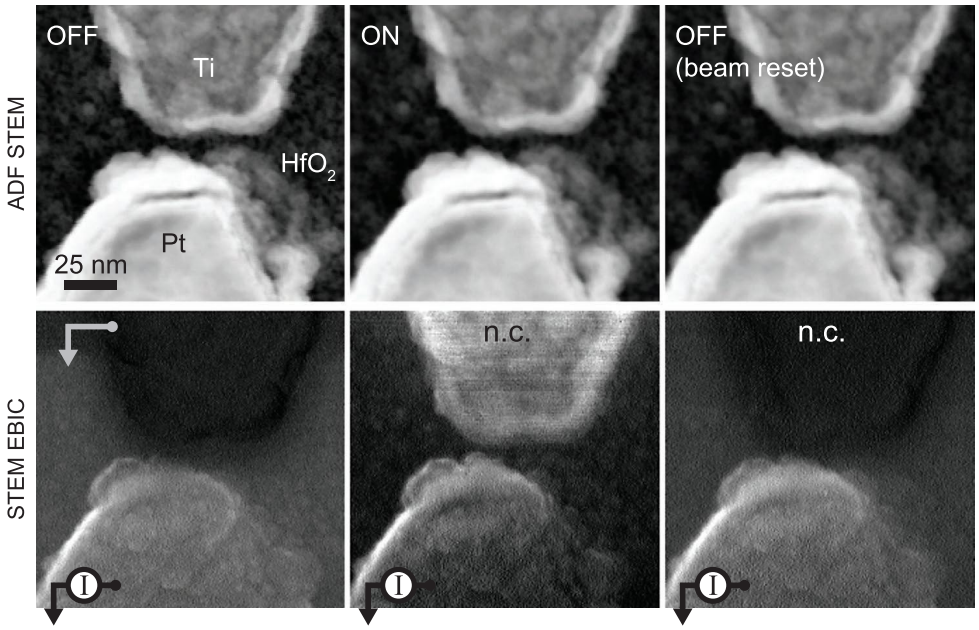

Figure 5. ON-state conduction switched OFF by STEM beam. Images acquired directly after a –10 V device RESET (left column) show negative EBIC from the Ti electrode, indicating that the device is OFF. With the beam blanked, the device is then SET and held at 9 V until immediately before another image acquisition (center column). The intermittent positive EBIC from the Ti electrode in this state indicates a non-ohmic connection to the Pt electrode. A final image (right column) immediately following shows only negative EBIC from the Ti electrode, indicating that the device has been RESET by the beam. ADF imaging (top row) shows no sign of these state changes, which are only made evident with EBIC imaging (bottom row). A "n.c." label on the Ti electrode indicates "no external connection".

bias and the Pt electrode is connected to the TIA. The Ti electrode is grounded when the device is nominally OFF (Figure 5, left column) and floating when nominally ON (Figure 5, center and right columns). After the RESET (SET) the Ti electrode is dark (bright) in the EBIC image, indicating that the Ti is not (is) connected to the Pt. However, the contrast on the floating Ti electrode, and only on the Ti electrode, is streaky when the device is ON (see also Figures S10 and S11, Supporting Information).

The streaking in the Ti is indicative of the device's nonlinear *I–V* relationship. As the beam rasters across the floating Ti electrode, pixel-by-pixel from left to right and line-by-line from top to bottom, SE ejection causes the Ti to charge positively. Eventually the charging produces a potential sufficient for PF conduction, and the Ti electrode then discharges into the Pt to produce positive (bright) EBIC. Immediately after a discharge the EBIC returns to a smaller value (gray). This charge/discharge cycle continues across the entire Ti electrode. Imaging with the frame rotated 180° (i.e., starting the raster on the Pt instead of the Ti) does not produce similar streaks on the Pt, which is directly connected to the TIA. (With the rotated scan direction the Ti appears dark for reasons to be discussed shortly.) While a hard filament is visible in this device (see also Figure S11, Supporting Information), this intermittent conduction is not consistent with an ohmic connection between electrodes. The voltage-dependent conduction is indicative of soft breakdown: this device is conducting through a PF soft filament in series with the ohmic hard filament during the first half of the ON-state images (Figure 5, second column).

To a degree not seen in Cu/Al_2O_3 CBRAM elements,[34] the VCM devices are beam sensitive, which suggests that this VCM chemistry may be unsuitable for radiation-hard applications and also provides clues as to the mechanisms underlying the ON state conduction. As the beam rasters through the gap (Figure 5, second column), SE emission produces holes that annihilate the injected electrons constituting the soft filament. As a result, images acquired immediately afterward (Figure 5, third column) and subsequent transport measurements show the device to be OFF. We find that electron beam exposure steadily increases the device resistance, eventually switching an ON device OFF (Figure S13, Supporting Information). Even a few seconds of exposure, as occurs while previewing the field of view prior to the longer EBIC image acquisition, typically returns a device in the LRS to the HRS. The change is especially rapid when the beam is imaging the region between the electrodes (Figure S12, Supporting Information). Transport in the beam-induced HRS more closely resembles the higher-resistance pre-forming state than the voltage-induced (i.e., deliberate RESET) HRS. The device can then be "reformed" into the ON state and will subsequently cycle normally.

Hard filaments are relatively robust to repeated EBIC image acquisition (Figure S14, Supporting Information). While an *I–V* shows that imaging an ON device switches it OFF, a second EBIC image shows the hard filament to be almost unchanged. The sensitivity of the device conductance to the beam, combined with the relative insensitivity of the hard filament to the beam, suggests that the beam primarily affects the soft portion of the ON-state filament. Imaging the filament with an electron beam ejects SE, leaving holes behind that annihilate trapped electrons[16] and destroy the soft filament, which RESETs the device. Devices which receive a large electron dose eventually fail into a persistent LRS; in the Figures 2 and 4 device switched reliably over dozens of cycles, failing after 40 EBIC images, each of which represents a dose of 3×10^6 nm^{-2}.

We understand our observations in terms of the following model (**Figure 6**). In a pristine device, the low density of oxygen vacancies in the ALD-deposited HfO_2 does not support electrical conduction between the Pt bottom electrode and the Ti top electrode.[43] The oxygen vacancies are present in a variety of charge states and aggregation numbers.[44,45] Applying a positive voltage bias to the top electrode injects electrons from the bottom electrode into nearby pre-existing vacancies.[42,46] These vacancies PF-conduct and constitute the soft filament, which grows (Figure 2) from the cathode (here the bottom electrode) independent of the electrode materials. With sufficient positive voltage bias, the soft filament eventually approaches the top electrode, producing a large electric field across the remaining gap (Figure 3). In this field some Ti is oxidized, creating new, positively-charged oxygen vacancies.[8,15,26,44] These positively-charged vacancies are especially mobile in the HfO_2 and are likely doubly-charged.[8,44,45] They drift in the *E*-field through the dielectric until they establish ohmic contact with the bottom electrode, where they are reduced. In sufficient concentration these oxygen vacancies dope the HfO_2 into ohmic conduction[15,26] and constitute the hard filament, which, like the soft filament, also grows up from the bottom electrode (Figure 4). This conducting filament growth resulting from positively-charged vacancies moving from the anode to the cathode is directly analogous to that seen with metal cations in CBRAM.[15,34] The cathode-to-anode growth direction indicates that the oxygen exchange rate at the Ti is slow compared to the vacancy migration through the HfO_2.[15] The vacancy transport and PF conduction currents generate Joule heating, which accelerates the transport and reaction rates and leads to positive feedback.[8,15] The creation of the hard filament, which generally does not span the entire gap between the electrodes, completes the forming process. With a current limit, as in VCM, the hard filament growth is regulated and the DB is controlled. With a voltage limit, as in a transistor or capacitor, positive feedback can produce uncontrolled, runaway DB and a catastrophic failure.

With hard and soft filaments in series, a small positive potential can drive an electrical current and the VCM device is in the ON state (Figures 4 and 5). Zeroing the applied bias causes the soft filament to retract from the top electrode as electrons return to the bottom electrode. Reversing the applied bias injects electrons from the other side, causing a soft filament to grow from the top electrode toward the bottom. Larger negative bias oxidizes the hard filament starting at its tip,[8] producing a RESET. Post-forming SET occurs at a lower voltage than the initial FORM (Figure 4) because of both trapped charge and the remaining hard filament.

This picture of DB in VCM makes a physical distinction between hard and soft breakdown, which historically have been difficult to distinguish:[2] the former involves the motion of atoms, ions, or vacancies, while the latter involves the motion of electrons or holes. As the motion of electrons is more easily reversed, to achieve the controllable, reversible DB required for memory function, at least part of the conducting filament in VCM should

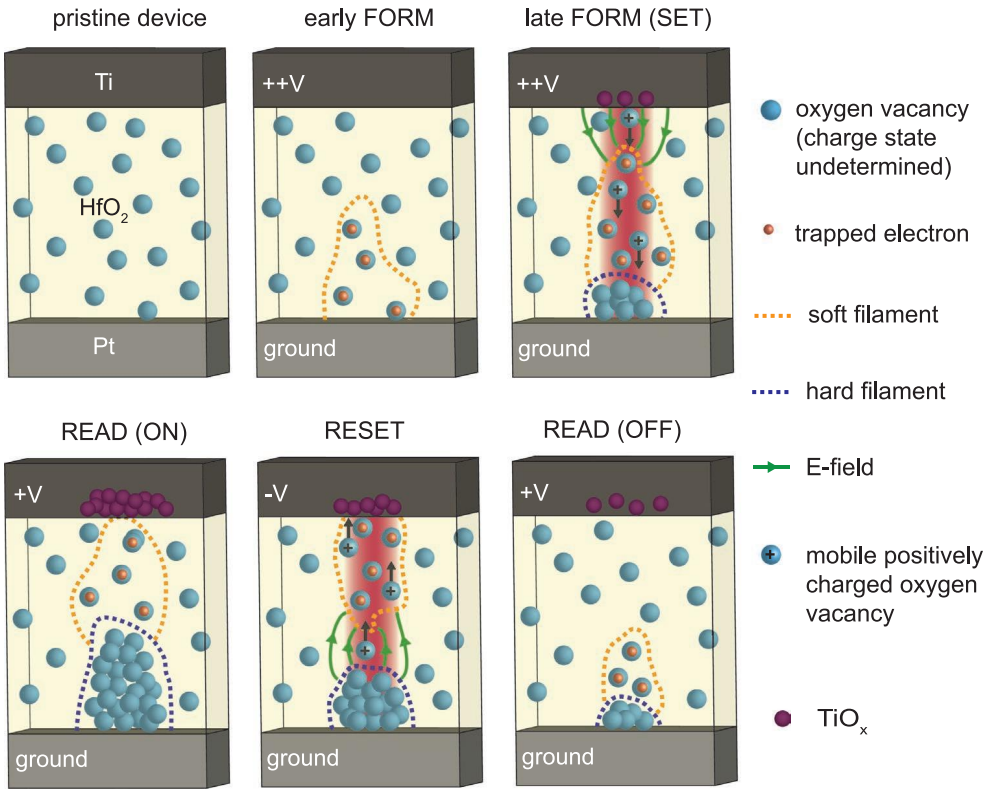

Figure 6. Model of the HfO_2 VCM switching process.[43] In Pt/HfO_2/Ti devices both hard and soft filaments are observed to grow from the bottom (Pt) electrode (cathode) toward the top (Ti) electrode (anode) during a SET.[13,14] STEM EBIC imaging visualizes all of this switching process's key features: the soft filament (Figure 2), the hard filament (Figure 4), the strong electric fields immediately preceding SET (Figure 3), and the charge-sensitive conduction mechanism (Figure 5).

be soft. Thus the ideal VCM ON-state represents an intermediate condition between the soft and hard breakdown limits; larger currents lead to harder breakdown, with thermal runaway and an unswitchable VCM device at the endpoint.[24] This DB picture moreover provides a clear theoretical framework that offers specific directives on how to optimize VCM switching parameters such as speed, retention, and longevity. During device fabrication the oxide density and its doping, for instance, might be independently tuned to separately address the ionic transport and electronic conduction, respectively, allowing direct control of the critical hard/soft filament length ratio. This model of DB is broadly consistent with previous findings, not only in HfO_2,[13,14,17] but also in other binary oxides such as TiO_2 and Ta_2O_5.[18,47–49]

Within the broader field of DB generally, these results provide a framework for understanding the distinction, or lack thereof, between hard and soft breakdown on the one hand, and (possibly time-dependent) progressive breakdown on the other.[2,3,8,50] With high-contrast, high-resolution imaging, hard and soft breakdown are physically distinguishable as described here, but without such imaging DB appears to occur on a progressive continuum, where the progression is measured by the unseen relative lengths of hard and soft filaments arranged in series.

Supporting Information

Supporting Information is available from the Wiley Online Library or from the authors.

Acknowledgements

W.A.H. and J.J.L. contributed equally to this work. The authors acknowledge helpful discussions with Gennadi Bersuker. This work was supported by the UCLA PSEIF, by National Science Foundation (NSF) Science and Technology Center (STC) award DMR-1548924 (STROBE), by NSF awards DMR-1611036 and DMR-2004897, and by the Semiconductor Research Corporation (SRC).

Conflict of Interest

The authors declare no conflict of interest.

Data Availability Statement

The data that support the findings of this study are available from the corresponding author upon reasonable request.

Keywords

device physics, dielectric breakdown, hafnium oxide, resistive random access memory, scanning transmission electron microscope electron beam induced current

Received: March 8, 2021
Revised: July 2, 2021
Published online:

[1] R. M. Wallace, in *Springer Handbook of Electronic and Photonic Materials* (Eds.: S. Kasap, P. Capper), Springer Handbooks, Springer International Publishing, Cham **2017**, pp. 615–644.
[2] F. Palumbo, C. Wen, S. Lombardo, S. Pazos, F. Aguirre, M. Eizenberg, F. Hui, M. Lanza, *Adv. Funct. Mater.* **2019**, *30*, 1900657.
[3] International Roadmap for Devices and Systems, Technical Report 2020, IEEE, **2020**, https://irds.ieee.org/ (accessed: November 2020).
[4] A. Padovani, L. Larcher, P. Padovani, C. Cagli, B. D. Salvo, in *2012 4th IEEE International Memory Workshop*, **2012**, pp. 1–4.
[5] M. Lanza, H.-S. P. Wong, E. Pop, D. Ielmini, D. Strukov, B. C. Regan, L. Larcher, M. A. Villena, J. J. Yang, L. Goux, A. Belmonte, Y. Yang, F. M. Puglisi, J. Kang, B. Magyari-Köpe, E. Yalon, A. Kenyon, M. Buckwell, A. Mehonic, A. Shluger, H. Li, T.-H. Hou, B. Hudec, D. Akinwande, R. Ge, S. Ambrogio, J. B. Roldan, E. Miranda, J. Suñe, K. L. Pey, et al., *Adv. Electron. Mater.* **2019**, *5*, 1800143.
[6] Z. Fang, H. Y. Yu, W. J. Liu, Z. R. Wang, X. A. Tran, B. Gao, J. F. Kang, *IEEE Electron Device Lett.* **2010**, *31*, 476.
[7] P. Gonon, M. Mougenot, C. Vallée, C. Jorel, V. Jousseaume, H. Grampeix, F. El Kamel, *J. Appl. Phys.* **2010**, *107*, 074507.
[8] G. Bersuker, D. C. Gilmer, D. Veksler, P. Kirsch, L. Vandelli, A. Padovani, L. Larcher, K. McKenna, A. Shluger, V. Iglesias, M. Porti, M. Nafría, *J. Appl. Phys.* **2011**, *110*, 124518.
[9] C. Walczyk, D. Walczyk, T. Schroeder, T. Bertaud, M. Sowinska, M. Lukosius, M. Fraschke, D. Wolansky, B. Tillack, E. Miranda, C. Wenger, *IEEE Trans. Electron Devices* **2011**, *58*, 3124.
[10] Y. S. Lin, F. Zeng, S. G. Tang, H. Y. Liu, C. Chen, S. Gao, Y. G. Wang, F. Pan, *J. Appl. Phys.* **2013**, *113*, 064510.
[11] A. S. Sokolov, Y.-R. Jeon, S. Kim, B. Ku, D. Lim, H. Han, M. G. Chae, J. Lee, B. G. Ha, C. Choi, *Appl. Surf. Sci.* **2018**, *434*, 822.
[12] Y. Yang, W. Lü, Y. Yao, J. Sun, C. Gu, L. Gu, Y. Wang, X. Duan, R. Yu, *Sc. Rep.* **2014**, *4*, 3890.
[13] B. Hudec, I.-T. Wang, W.-L. Lai, C.-C. Chang, P. Jančovič, K. Fröhlich, M. Mičušík, M. Omastová, T.-H. Hou, *J. Phys. D: Appl. Phys.* **2016**, *49*, 215102.
[14] C. Li, B. Gao, Y. Yao, X. Guan, X. Shen, Y. Wang, P. Huang, L. Liu, X. Liu, J. Li, C. Gu, J. Kang, R. Yu, *Adv. Mater.* **2017**, *29*, 1602976.
[15] S. Menzel, R. Waser, in *Advances in Non-Volatile Memory and Storage Technology*, 2nd ed. (Eds.: B. Magyari-Köpe, Y. Nishi), Woodhead Publishing Series in Electronic and Optical Materials, Woodhead Publishing, Cambridge **2019**, pp. 137–170.
[16] V. A. Gritsenko, T. V. Perevalov, D. R. Islamov, *Phys. Rep.* **2016**, *613*, 1.
[17] D. S. Jeong, H. Schroeder, U. Breuer, R. Waser, *J. Appl. Phys.* **2008**, *104*, 123716.
[18] J. J. Yang, F. Miao, M. D. Pickett, D. A. A. Ohlberg, D. R. Stewart, C. N. Lau, R. S. Williams, *Nanotechnology* **2009**, *20*, 215201.
[19] U. Celano, J. Op de Beeck, S. Clima, M. Luebben, P. M. Koenraad, L. Goux, I. Valov, W. Vandervorst, *ACS Appl. Mater. Interfaces* **2017**, *9*, 10820.
[20] N. Raghavan, K. L. Pey, K. Shubhakar, *Microelectron. Reliab.* **2014**, *54*, 847.
[21] A. Wedig, M. Luebben, D.-Y. Cho, M. Moors, K. Skaja, V. Rana, T. Hasegawa, K. K. Adepalli, B. Yildiz, R. Waser, I. Valov, *Nat. Nanotechnol.* **2016**, *11*, 67.
[22] D.-H. Kwon, K. M. Kim, J. H. Jang, J. M. Jeon, M. H. Lee, G. H. Kim, X.-S. Li, G.-S. Park, B. Lee, S. Han, M. Kim, C. S. Hwang, *Nat. Nanotechnol.* **2010**, *5*, 148.
[23] B. D. Hoskins, G. C. Adam, E. Strelcov, N. Zhitenev, A. Kolmakov, D. B. Strukov, J. J. McClelland, *Nat. Commun.* **2017**, *8*, 1972.
[24] J. Meng, B. Zhao, Q. Xu, J. M. Goodwill, J. A. Bain, M. Skowronski, *J. Appl. Phys.* **2020**, *127*, 235107.
[25] S. Kumar, C. E. Graves, J. P. Strachan, E. M. Grafals, A. L. D. Kilcoyne, T. Tyliszczak, J. N. Weker, Y. Nishi, R. S. Williams, *Adv. Mater.* **2016**, *28*, 2772.
[26] M. Sowinska, T. Bertaud, D. Walczyk, S. Thiess, M. A. Schubert, M. Lukosius, W. Drube, C. Walczyk, T. Schroeder, *Appl. Phys. Lett.* **2012**, *100*, 233509.
[27] J. Kwon, A. A. Sharma, C.-Y. Chen, A. Fantini, M. Jurczak, A. A. Herzing, J. A. Bain, Y. N. Picard, M. Skowronski, *ACS Appl. Mater. Interfaces* **2016**, *8*, 20176.
[28] D. Cooper, C. Baeumer, N. Bernier, A. Marchewka, C. L. Torre, R. E. Dunin-Borkowski, S. Menzel, R. Waser, R. Dittmann, *Adv. Mater.* **2017**, *29*, 1700212.
[29] J.-Y. Chen, C.-W. Huang, C.-H. Chiu, Y.-T. Huang, W.-W. Wu, *Adv. Mater.* **2015**, *27*, 5028.
[30] S. Privitera, G. Bersuker, B. Butcher, A. Kalantarian, S. Lombardo, C. Bongiorno, R. Geer, D. C. Gilmer, P. D. Kirsch, *Microelectron. Eng.* **2013**, *109*, 75.
[31] J. Yao, L. Zhong, D. Natelson, J. M. Tour, *Sci. Rep.* **2012**, *2*, 242.
[32] G.-S. Park, Y. B. Kim, S. Y. Park, X. S. Li, S. Heo, M.-J. Lee, M. Chang, J. H. Kwon, M. Kim, U.-I. Chung, R. Dittmann, R. Waser, K. Kim, *Nat. Commun.* **2013**, *4*, 2382
[33] C. Kittel, *Introduction to Solid State Physics*, 8th ed., Wiley, Hoboken, NJ **2005**.
[34] W. A. Hubbard, A. Kerelsky, G. Jasmin, E. R. White, J. Lodico, M. Mecklenburg, B. C. Regan, *Nano Lett.* **2015**, *15*, 5665.
[35] T. E. Everhart, O. C. Wells, R. K. Matta, *Proc. IEEE* **1964**, *52*, 1642.
[36] H. J. Leamy, *J. Appl. Phys.* **1982**, *53*, R51.
[37] W. A. Hubbard, M. Mecklenburg, H. L. Chan, B. C. Regan, *Phys. Rev. Appl.* **2018**, *10*, 044066.
[38] W. A. Hubbard, Z. Lingley, J. Theiss, S. Sitzman, T. Ayvazian, M. Brodie, B. Foran, *Appl. Phys. Lett.* **2019**, *115*, 133502.
[39] M. Mecklenburg, W. A. Hubbard, J. J. Lodico, B. C. Regan, *Ultramicroscopy* **2019**, *207*, 112852.
[40] M. A. Alam, B. E. Weir, P. J. Silverman, *IEEE Trans. Electron Devices* **2002**, *49*, 232.
[41] M. Houssa, P. Mertens, M. Heyns, J. Jeon, A. Halliyal, B. Ogle, *Solid-State Electron.* **2000**, *44*, 521.
[42] C. Goldsmith, J. Ehmke, A. Malczewski, B. Pillans, S. Eshelman, Z. Yao, J. Brank, M. Eberly, *IEEE MTT-S Int. Microwave Symp. Dig.* **2001**, 227.
[43] We refrain from labeling the charge state, aggregation number, or mobility for oxygen vacancies when such information is not provided by our data. Thus, unless otherwise indicated, we do not mean to suggest that the solitary vacancies in Figure 6 are, for example, either neutral or charged (either before or after electron injection), or single, di-, or trivacancies.
[44] S. R. Bradley, G. Bersuker, A. L. Shluger, *J. Phys.: Condens. Matter* **2015**, *27*, 415401.
[45] M. P. Mueller, F. Gunkel, S. Hoffmann-Eifert, R. A. De Souza, *J. Appl. Phys.* **2021**, *129*, 025104.
[46] W. Zhu, T. Ma, S. Zafar, T. Tamagawa, *IEEE Electron Device Lett.* **2002**, *23*, 597.
[47] A. A. Sharma, M. Noman, M. Abdelmoula, M. Skowronski, J. A. Bain, *Adv. Funct. Mater.* **2014**, *24*, 5522.
[48] K. M. Kim, B. J. Choi, Y. C. Shin, S. Choi, C. S. Hwang, *Appl. Phys. Lett.* **2007**, *91*, 012907.
[49] J. H. Yoon, S. J. Song, I.-H. Yoo, J. Y. Seok, K. J. Yoon, D. E. Kwon, T. H. Park, C. S. Hwang, *Adv. Funct. Mater.* **2014**, *24*, 5086.
[50] E. Y. Wu, *IEEE Trans. Electron Devices* **2019**, *66*, 4535.